(Received 7 August 2025, Accepted 15 November 2025, Scheduled 23 November 2025)

Electromagnetic-Thermal Coupling in Sliding Contacts: Modeling Dynamic Resistance and Heat Generation for Electromagnetic Launch Systems

Yikang Song[1,2], Pengyu Li[1,*], Junsheng Cheng[1,2], and Heyang Wang[3]

[1]*Institute of Electrical Engineering, Chinese Academy of Sciences, Beijing 100190, China*
[2]*University of Chinese Academy of Sciences, Beijing 100049, China*
[3]*North China Electric Power University, Beijing 102206, China*

ABSTRACT: This study addresses multi-physics coupling challenges in high-speed sliding electrical contacts for Electromagnetic Launch Systems. A three-dimensional transient finite element model integrating electromagnetic-thermal interactions is established. By combining modified adhesion theory with Holm's contact resistance theory, we derive an analytical expression for dynamic contact resistance (DCR) that incorporates electromagnetic contact pressure, tangential friction, and temperature-dependent conductivity. The proposed localized modeling strategy with rail reverse motion technique efficiently resolves armature motion through coordinate transformation. Governing equations are discretized via the Galerkin method, with interfacial current continuity constraints and thermal partition coefficients enabling precise separation of Joule heating and frictional heat. Numerical results demonstrate robust current continuity compliance and reveal that DCR reaches its minimum during current peaks, exhibiting strong negative correlation with electromagnetic thrust. Tangential friction suppresses resistance rise by expanding the actual contact area, while electromagnetically dominated skin effects generate localized hotspots at contact trailing edges, armature limbs, and throat regions. This work elucidates the coupled frictional-Joule heating mechanisms governing multi-physics interactions, providing critical foundations for thermal management optimization in Electromagnetic Launch Systems.

1. INTRODUCTION

Pulsed high-current electromagnetic launch systems have garnered substantial research interest due to their superior ballistic performance [1, 2]. During high-speed sliding, electrical contact between the armature and rails is maintained through discrete conducting spots at asperity junctions, where localized plastic deformation forms micro-welded interfaces [3]. Sustaining optimal sliding contact performance is thus a critical prerequisite for achieving high-efficiency operation in such systems [4]. Critically, the dynamic contact resistance (DCR) characterizes the evolution of interfacial contact conditions throughout the launch process, offering profound insights for enhancing system performance and longevity [5–7].

The electromagnetic-thermal coupling at the armature-rail interface induces complex thermal loading, comprising two principal components [8, 9]. First, substantial interfacial Joule heating arises from current flow through significant contact resistance. Second, frictional heating is generated by high-speed armature sliding. This composite heat source dynamically partitions between components: a portion propagates into the armature's contact surface, with the remainder transferring to the rail's contact surface.

Concurrently, bulk Joule heating within the contact zone — resulting from current conduction through resistive materials — further elevates temperatures [10]. Under combined interfacial and bulk heating, the contact material undergoes rapid temperature rise and potential melting.

Prior studies on electromagnetic-thermal coupling in sliding contacts exhibit significant limitations in resolving dynamic interactions: Ref. [11] derived fundamental electro-magneto-thermal equations yet simplified contact resistance as a lumped thermal source, failing to capture its spatiotemporal evolution; Ref. [12] developed a transient multiphysics solver for armature temperatures but assumed perfect contact conditions, thereby neglecting interfacial heat partitioning mechanisms critical for thermal management. Similarly, a recent multi-physics prognostic model for bond wire lift-off [13] also highlights the critical impact of uneven temperature distribution on degradation, yet its focus remains on a different physical interface and does not address the high-speed sliding coupling central to our work. Although empirical dynamic contact resistance (DCR) data were acquired in [14] and wear dynamics analyzed in [15], both relied on analytical approximations for interfacial heat flux that cannot resolve coupled electromagnetic-thermal transients. Similarly, static contact tests in [16] and indirect resistance measurements in [17] were inherently incapable of probing high-speed sliding coupling due to their quasi-static methodologies.

* Corresponding author: Pengyu Li (syk785817@163.com).

In summary, existing methodologies fail to establish a fully coupled electromagnetic-thermal framework capable of simultaneously quantifying DCR evolution and interfacial heat partitioning under high-speed sliding. To address this gap, we conduct comprehensive numerical simulations on a C-shaped armature, incorporating: A 3D transient finite element model integrating electromagnetic-thermal interactions; Analytical DCR formulation combining modified adhesion theory and Holm's contact theory; Localized interfacial heat loading with thermal partition coefficients; Rail reverse motion technique for efficient dynamic simulation.

This work scrutinizes current distribution, magnetic fields, temperature profiles, electromagnetic forces, and DCR evolution. Crucially, it elucidates the fundamental electromagnetic-thermal coupling mechanisms governing interfacial heat generation and resistance dynamics — providing critical foundations for thermal management in electromagnetic launch systems.

2. ELECTROMAGNETIC-THERMAL COUPLED MODELING OF DYNAMIC CONTACT RESISTANCE

2.1. Armature-rail Interface Heat Model

The interfacial heat source comprises both contact-resistance-induced Joule heating and sliding-friction-generated heat at the interface [18]. During sliding, this heat source continuously acts on the contact interface. Relative to the armature, it constitutes a stationary heat source, whereas for the rail, the heat source is localized at the contact zone and thus represents a traveling heat source [19]. A schematic diagram of the high-speed sliding process between the armature and rail is presented in Figure 1.

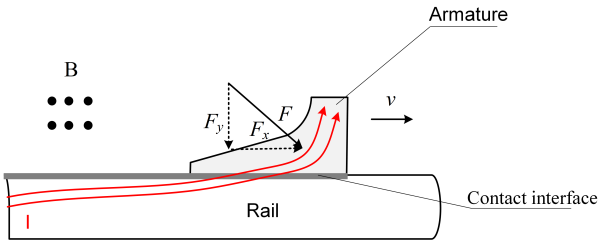

FIGURE 1. Schematic diagram of armature/rail electromagnetic contact pressure.

Since the armature sliding duration is sufficiently brief, convective heat transfer with ambient air can be considered negligible. Heat transfer occurs exclusively through conduction. We further assume no interfacial heat loss to the environment — all generated heat at the contact interface is entirely absorbed by the rail and armature.

2.2. Dynamic Contact Resistance Formulation

During electromagnetic launch operations, the contact pressure distribution at the armature-rail interface is nonuniform. The actual contact state between armature and rail significantly deviates from the ideal contact configuration [20]. The total contact force F_c, which comprises both the electromagnetic force (Lorentz force) and an initial mechanical preload, is essential for maintaining contact. This initial preload, applied during armature insertion, ensures proper electrical contact and inevitably causes elastic deformation of the armature, breaking the geometric symmetry and resulting in a net normal force [21]. Figure 2 illustrates the contact morphology at the microstructural level, where R_c = Contact resistance, R_m = Bulk conductor resistance, F_c = Total contact force.

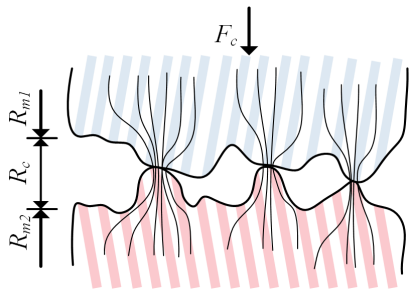

FIGURE 2. Contact interface at the microscopic scale.

Contact resistance depends on factors including contact pressure, contact area, and material hardness. Prior to armature transition, this resistance typically remains within the range of 10^{-6} to $10^{-3}\,\Omega$ [22].

The contact resistance $R_c(t)$ comprises the oxide film resistance and constriction resistance $R_s(t)$. During armature insertion into the rail, surface oxide films are disrupted by friction, hence $R_c(t) = R_s(t)$.

Constriction resistance incorporates temperature dependence:

$$\rho(T) = \rho_0 \left[1 + \alpha(T - T_0)\right] \tag{1}$$

where ρ_0 is the initial electrical resistivity, ΔT the temperature rise, and α the temperature coefficient of resistivity.

According to Holm's theory, the constriction resistance for a single contact spot (radius a) is:

$$R_{si}^{'}(t) = \frac{\rho_1(t) + \rho_2(t)}{4a_i} \tag{2}$$

$\rho_1(t)$, $\rho_2(t)$ denote the resistivities of the armature and rail, respectively. For a contact interface containing n uniform contact spots (each with radius a), the total contact resistance is:

$$R_c(t) = R_s(t) = \frac{\rho_1(t) + \rho_2(t)}{4\sum a_i} = \frac{\rho_1(t) + \rho_2(t)}{4na} \tag{3}$$

Effective contact area $A_c^{'}$ relates to contact pressure F_c:

$$A_c = \eta \frac{F_c}{\sigma_y} \tag{4}$$

σ_y is the yield point of the softer material, and η is a correction factor.

Under sliding friction conditions, contact spot deformation results from the combined action of normal compressive stress σ and tangential shear stress τ. Based on the modified adhesion theory, the equivalent stress satisfies:

$$\sigma^2 + \varepsilon\tau^2 = k^2 \tag{5}$$

$\varepsilon > 1$, k is the equivalent stress. In the static friction state ($\tau = 0$), $\sigma = \sigma_s$, thus $k = \sigma_s$:

$$\sigma^2 + \varepsilon\tau^2 = \sigma_s^2 \tag{6}$$

Substituting the stress definitions ($\sigma = \eta F_c/A_c^{'}$, $\tau = F_f/A_c^{'}$, where F_f is the friction force):

$$\left(\eta\frac{F_c}{A_c^{'}}\right)^2 + \varepsilon\left(\frac{F_f}{A_c^{'}}\right)^2 = \sigma_s^2 \tag{7}$$

Solving for the effective contact area $A_c^{'}$ yields:

$$A_c^{'} = \sqrt{\left(\eta\frac{F_c}{\sigma_s}\right)^2 + \varepsilon\left(\frac{F_f}{\sigma_s}\right)^2} \tag{8}$$

For most metallic materials, $\tau = 0.2\sigma_s$ holds, leading to $\varepsilon = 25$. The term $\eta\frac{F_c}{\sigma_s}$ represents the static friction contact area, while $\varepsilon\left(\frac{F_f}{\sigma_s}\right)^2$ accounts for the area increase due to tangential force.

Assuming identical and uniformly distributed contact spots ($A_c^{'} = n\pi a^2$) and combining Equation (3) with Equation (8), the contact resistance model is derived:

$$R_c(t) = \frac{\rho_1(t) + \rho_2(t)}{4}\left(\frac{\pi^2\sigma_s^2}{n^2\left(\eta^2F_c^2 + \varepsilon F_f^2\right)}\right)^{\frac{1}{4}} \tag{9}$$

This model integrates the effects of contact pressure F_c, tangential force F_f, material hardness σ_s, and contact spot parameters (η, n, ε), offering enhanced accuracy compared to models employing a constant contact resistance value.

3. DYNAMIC ELECTROMAGNETIC FIELD MODELING WITH MOVING CONDUCTORS

3.1. Electromagnetic Governing Equations

A-φ method is employed for electromagnetic field computation in electromagnetic launch systems. The Coulomb gauge ($\nabla \cdot \vec{\mathbf{A}} = 0$) is imposed to ensure the uniqueness of the magnetic vector potential $\mathbf{A}$. The weak form of the governing equations is:

$$\int_V \left(\frac{1}{\mu}\nabla\times\mathbf{W}_j\cdot\nabla\times\mathbf{A} + \frac{1}{\mu}\nabla\cdot\mathbf{W}_j\nabla\cdot\mathbf{A} + \sigma\mathbf{W}_j\cdot\nabla\varphi + \sigma\mathbf{W}_j\cdot\frac{\partial\mathbf{A}}{\partial t}\right)dV = 0 \tag{10}$$

$$\int_V \nabla N_j\cdot\left(\sigma\nabla\varphi + \sigma\frac{\partial\mathbf{A}}{\partial t}\right)dV = 0 \tag{11}$$

where μ is the permeability, σ the conductivity, and $\mathbf{W}_j, \mathbf{N}_j$ are weighting functions.

The solution domain is discretized into finite elements. Within each element, the field quantities are approximated using shape functions W_k:

$$\vec{A}^e = \sum_{k=1}^{\theta_0} W_k\vec{A}_k, \quad \varphi^e = \sum_{k=1}^{\theta_0} W_k\varphi_k \tag{12}$$

Substituting into the governing equations and assembling into the global system yields:

$$\mathbf{K}\begin{pmatrix}A_x\\A_y\\A_z\\\varphi\end{pmatrix} + \mathbf{C}\frac{\partial}{\partial t}\begin{pmatrix}A_x\\A_y\\A_z\\\varphi\end{pmatrix} = \mathbf{0} \tag{13}$$

where K is the stiffness matrix, and C is the damping (dynamic) matrix.

Time discretization is performed using the backward Euler method (unconditionally stable):

$$\left[\mathbf{K} + \frac{\mathbf{C}}{\Delta t}\right][\mathbf{A}_\varphi]^{t+\Delta t} = \left[\frac{\mathbf{C}}{\Delta t}\right][\mathbf{A}_\varphi]^t \tag{14}$$

where $\mathbf{A}_\varphi = [\mathbf{A}_x, \mathbf{A}_y, \mathbf{A}_z, \varphi]^T$ and Δt is the time step.

Post-processing yields the magnetic flux density B and current density J:

$$\begin{cases} B_{kx}^e = \sum\limits_{k=1}^{e_0}\left(\frac{\partial W_k}{\partial y}A_{kz} - \frac{\partial W_k}{\partial z}A_{ky}\right) \\ J_{kx}^{e,t+\Delta t} = -\sigma\sum\limits_{k=1}^{e_0}\left(\frac{\partial W_k}{\partial x}\varphi_k^{t+\Delta t} + W_k\frac{A_{kx}^{t+\Delta t} - A_{kx}^t}{\Delta t}\right) \end{cases} \tag{15}$$

The electromagnetic force is computed via the Lorentz force law:

$$\vec{F} = \int_V (J\times B)\,dV \tag{16}$$

The X-component (F_x) is utilized for dynamic analysis, while the y-component (F_y) is used for contact interface normal load analysis.

3.2. Rail Reverse Motion Technique for Dynamic Simulation

The rail reverse motion technique is adopted to efficiently handle the armature's motion without remeshing. In this approach, the rail is assigned a velocity opposite to the armature's physical velocity, making the armature stationary relative to the computational domain. This coordinate transformation simplifies the dynamic simulation by eliminating convective terms and suppressing numerical oscillations.

The implementation of this technique requires a special treatment for the temporal derivatives of field quantities at points within the moving rail domain. For a point P on a moving conductor, the temporal derivative of freedom U is discretized as [12]:

$$\frac{dU(X,Y)}{dt} = \frac{U^{t+\Delta t}(x_2,y_2) - U^t(x_1,y_1)}{\Delta t} \tag{17}$$

where (x_1, y_1) and (x_2, y_2) denote coordinates of P in the fixed frame at t and $t + \Delta t$, respectively. Calculation requires U at time t. This coordinate transformation relationship is illustrated in Figure 3.

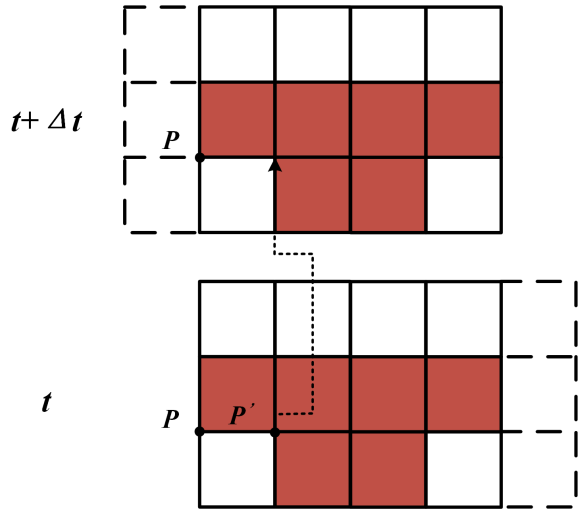

FIGURE 3. Coordinate transformation for moving conductors.

3.3. Electromagnetic-Thermal Contact Interface Conditions

The armature and adjacent air are stationary (Eulerian); the rail and adjacent air form a moving domain (Lagrangian). The moving domain translates opposite to the physical motion direction, eliminating velocity terms in governing equations to suppress numerical oscillation [23, 24].

Contact Interface Conditions:

$$A_m = A_s \tag{18}$$

$$\varphi_m - \varphi_s = v \cdot A_m + r_c \cdot (n \cdot J) \tag{19}$$

where r_c is the contact resistance per unit area, J the current density, v the velocity (X-direction), and subscripts m/s the moving/static nodes.

Owing to the geometric and electromagnetic symmetry of the system, a quarter-model is adopted to enhance computational efficiency. At the central symmetry plane, a magnetic symmetry boundary condition is imposed. This condition is enforced by setting the tangential components of the magnetic vector potential to zero:

$$n \times A = 0 \tag{20}$$

where n is the normal vector to the symmetry plane. Physically, this condition implies that the magnetic field lines are parallel to the symmetry plane, and the normal component of the magnetic flux density is zero [25, 26]. The implementation of the rail reverse motion technique requires a corresponding adjustment to the boundary conditions at the current-injecting rail end. As the rail domain is artificially translated, this end face can no longer be treated as a conventional equipotential surface. To ensure physical consistency and current continuity under this coordinate transformation, the following constraint is imposed:

$$\frac{\partial \varphi}{\partial i} + \frac{\partial A_i}{\partial t} = 0 \quad (i = y, z) \tag{21}$$

Constraints are enforced via the penalty method and integrated into the global matrix equation.

4. THERMAL MODELING

4.1. Thermal Governing Equations with Joule Heating Sources

The transient temperature field is governed by Fourier's law with interfacial and volumetric Joule heat sources:

$$\int_V \lambda \nabla N_j \cdot \nabla T \mathrm{d}V + \int_V \rho c \frac{\partial T}{\partial t} N_j \mathrm{d}V = \int_V \frac{J^2}{\sigma} N_j \mathrm{d}V \tag{22}$$

where T is the temperature, ρ the density, c the specific heat, and λ the thermal conductivity.

Element discretization yields the matrix equation:

$$[\mathbf{K}_T^e][\mathbf{T}^e] + [\mathbf{M}_T^e]\frac{\partial}{\partial t}[\mathbf{T}^e] = [\mathbf{Q}_T^e] \tag{23}$$

with: $K_{Tjk}^e = \int_{V^e} \lambda \left(\frac{\partial N_j}{\partial x}\frac{\partial N_k}{\partial x} + \frac{\partial N_j}{\partial y}\frac{\partial N_k}{\partial y} + \frac{\partial N_j}{\partial z}\frac{\partial N_k}{\partial z} \right) \mathrm{d}V$ (Conductivity matrix), $M_{Tjk}^e = \int_{V^e} \rho c N_j N_k \mathrm{d}V$ (Capacity matrix), $Q_{Tj}^e = \int_{V^e} \frac{|J^e|^2}{\sigma} N_j \mathrm{d}V$ (Heat source vector).

Time discretization is performed using the backward Euler method:

$$\left[\mathbf{K}_T + \frac{\mathbf{M}_T}{\Delta t}\right][\mathbf{T}_T]^{t+\Delta t} = \left[\frac{\mathbf{M}_T}{\Delta t}\right][\mathbf{T}_T]^t + [\mathbf{Q}_T]^t \tag{24}$$

4.2. Interfacial Heat Partitioning and Boundary Conditions

Adiabatic boundary conditions are imposed on all external surfaces (including air-domain interfaces), with zero normal heat flux at symmetric planes:

$$-k \left.\frac{\partial T}{\partial n}\right|_{\Gamma_{\text{external}}} = 0 \tag{25}$$

Interfacial heat sources during sliding electrical contact are applied as follows:

Friction heat as surface flux density:

$$Q_f(t) = \mu_f P_n(t) v(t) \tag{26}$$

Contact Joule heat as discrete nodal sources:

$$Q_{ci}(t) = I_i^2(t) R_{ci}(t) \tag{27}$$

where μ_f is the friction coefficient, $P_n(t)$ the contact pressure, $R_{ci}(t)$ the contact resistance at node i, and $I_i(t)$ the shunted current.

Heat partition coefficients η_r (rail side) and η_a (armature side) govern interfacial heat distribution:

$$\begin{cases} \eta_r = \frac{\sqrt{\lambda_r \rho_r c_r}}{\sqrt{\lambda_r \rho_r c_r} + \sqrt{\lambda_a \rho_a c_a}} \\ \eta_a = \frac{\sqrt{\lambda_a \rho_a c_a}}{\sqrt{\lambda_r \rho_r c_r} + \sqrt{\lambda_a \rho_a c_a}} \end{cases} \tag{28}$$

where ρ is the density, c the specific heat, λ the thermal conductivity, and $\eta_r + \eta_a = 1$.

Equation (28) provides the steady-state heat partition coefficient based on the thermal effusivity of the materials, which determines the initial split of heat flux at a contact interface. It offers a reasonable first-order approximation for the intense, transient heating process by ensuring that more heat flows into the material with higher ability to absorb it.

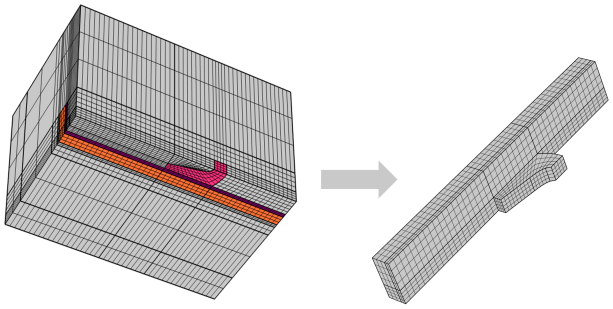

FIGURE 4. Schematic diagram of the solution model.

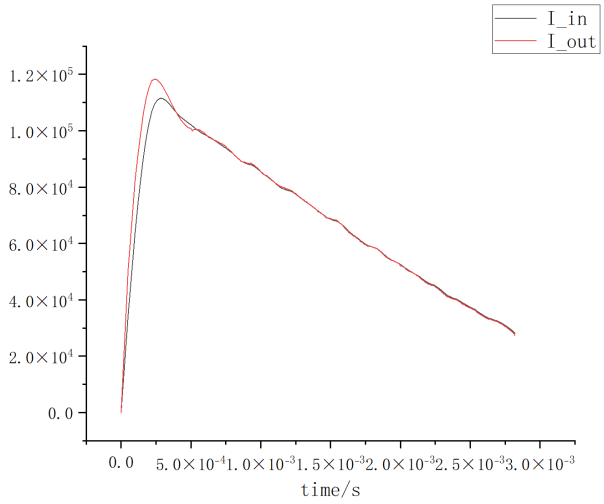

FIGURE 5. Comparison of input current and computed armature current.

5. ELECTROMAGNETIC-DRIVEN ARMATURE DYNAMICS

The aerodynamic resistance on the armature is given by:

$$F_k = 1.1\rho_0 S v^2 \tag{29}$$

where ρ_0 is the air density, S the frontal area of the armature, and v the velocity.

The kinematic parameters of the armature are determined by solving electromagnetic thrust, friction, and aerodynamic forces:

$$v = \int_0^t \frac{F_x - F_f - F_k}{m} \mathrm{d}t \tag{30}$$

$$x = x_0 + \int_0^t v \mathrm{d}t \tag{31}$$

Here F_x is the electromagnetic thrust along the sliding direction, F_f the friction force, m the constant armature mass, x the displacement, and x_0 the initial position.

6. NUMERICAL RESULTS AND DISCUSSION

Owing to the symmetry of the model, a quarter-symmetry configuration was adopted to reduce computational cost.

The finite-length modeling domain is optimized to capture the essential electromagnetic-thermal interactions around the armature, particularly the velocity skin effect. The total physical rail length in our system is 2 m, and the dynamic simulation covers the entire acceleration process along this length, with the armature achieving a final displacement of 2 m.

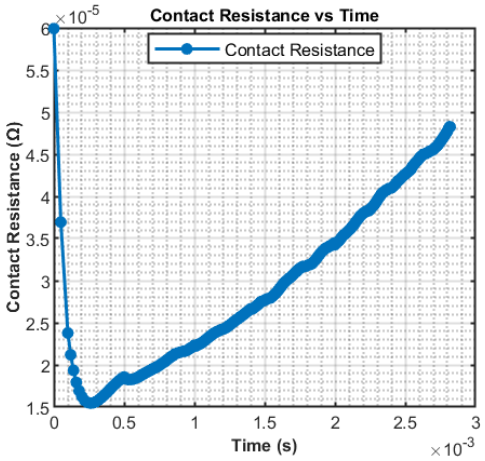

FIGURE 6. Dynamic contact resistance values.

TABLE 1. Material parameters of the model.

Parameter	6061 Aluminum Alloy	Copper
c/J·(kg·K)$^{-1}$	896	385
μ/H·m^{-1}	1.2566e-6	1.2566e-6
λ/W·(m·K)$^{-1}$	167	385
α/K	0.0041	0.0039
σ_0/MS·m^{-1}	25.0	58.5
T_0/K	300.00	300.00
T_m/K	924.85	1356.15
ρ/kg·m^{-3}	2700	8960

The computational model, shown in Figure 4, was discretized using eight-node hexahedral elements. The solution domain comprises 18,020 conductor elements and 64,307 nodes. The armature is aluminum (10 g mass), while the rails are copper. Material properties of metals are summarized in Table 1.

The dynamic simulation spanned a total duration of 2.8 ms with preset time steps, where the minimum step size was 15 μs. Impressed pulsed current excitation was applied to the left end-face of the rail.

As depicted in Figure 5, the current reaches a peak amplitude of 109 kA at 0.3 ms before decaying to a final level of 27.7 kA. To quantify current continuity compliance, the relative error between the input and computed armature currents was evaluated. This error was found to remain below 4% throughout the simulation, reaching a maximum of 3.71% at 0.28 ms. These results provide strong numerical validation for the method's accuracy in preserving current continuity.

As illustrated in Figure 6, the contact resistance reaches its minimum at approximately 0.3 ms. It then increases gradually during the current flat-top phase and initial falling-edge period, followed by accelerated growth in the later stage of the current falling edge. Notably, the computed contact resistance exhibits an inverse correlation trend with the electromagnetic force variation shown in Figure 7, as theoretically expected.

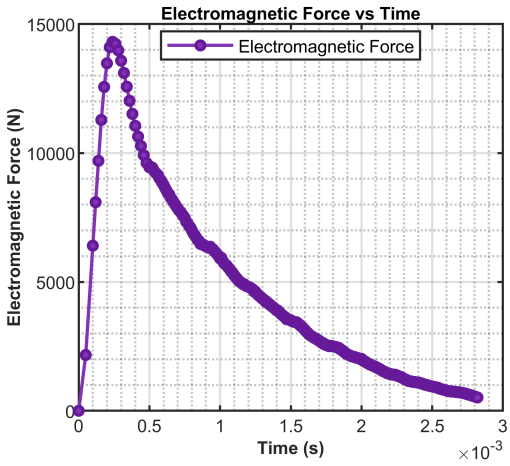

FIGURE 7. Electromagnetic force.

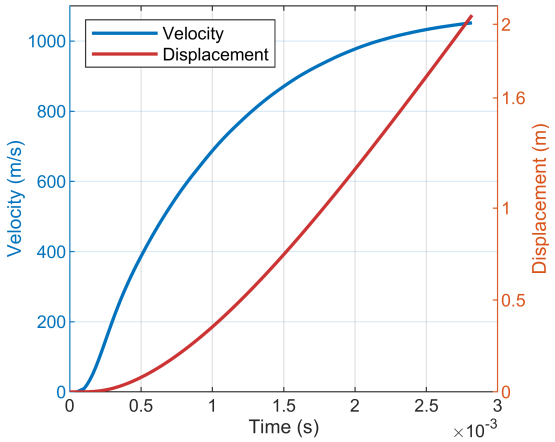

FIGURE 8. Velocity and displacement.

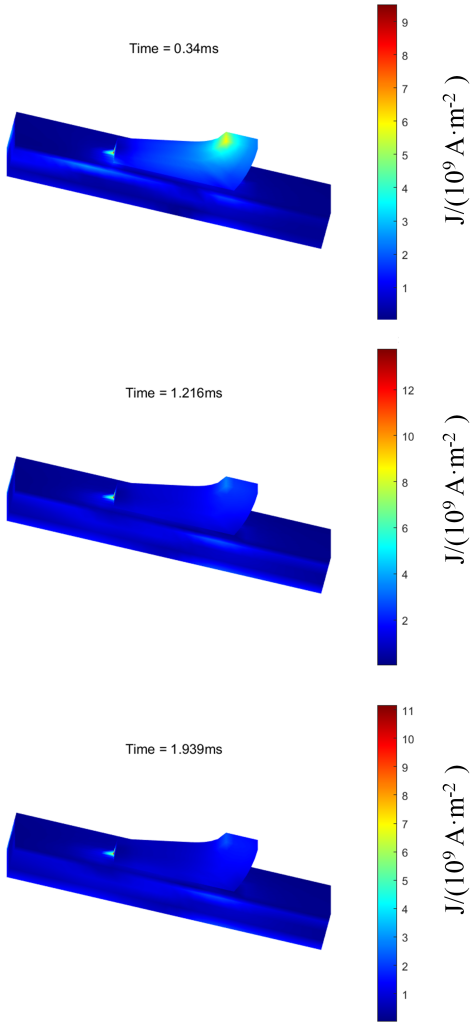

FIGURE 9. Evolution of current density.

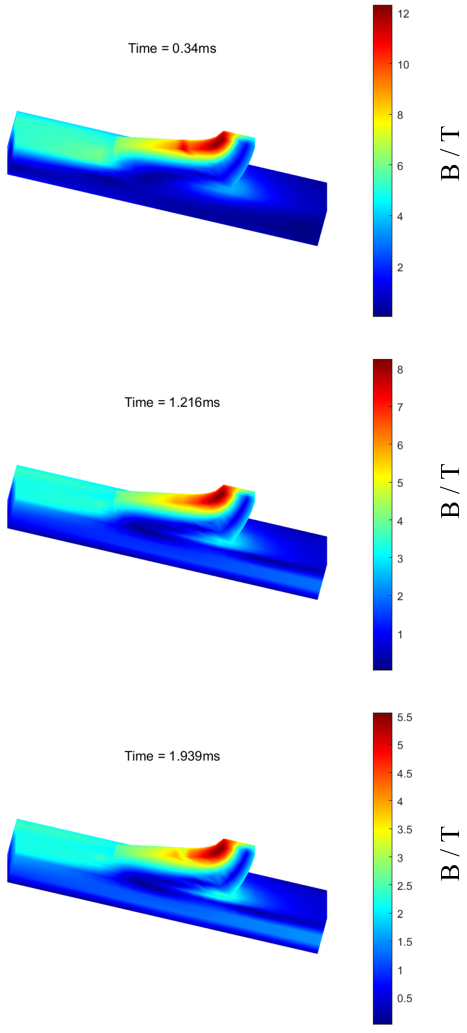

FIGURE 10. Evolution of magnetic induction.

As shown in Figure 8, the computed armature velocity reaches 1048.24 m/s at 2.8 ms with 2 m displacement. During the current rising edge, velocity increases steeply, while during the falling edge it rises steadily until armature ejection at 2 m displacement.

During the sliding electrical contact process, the electromagnetic field evolution in the armature-rail system is depicted in Figures 9–11. As velocity increases, the Velocity Skin Effect (VSE) becomes increasingly pronounced. Current progressively concentrates on the rail surface, with peak current den-

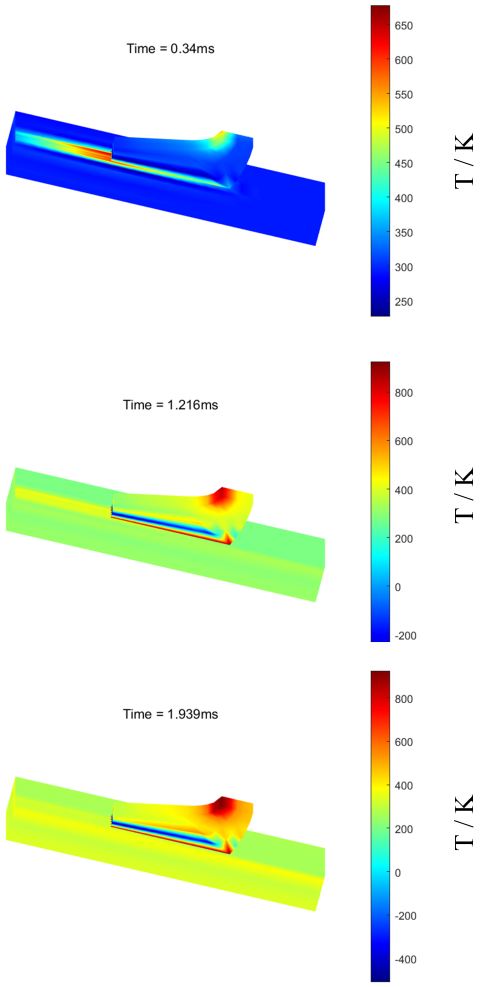

FIGURE 11. Evolution of temperature.

sity occurring at the trailing edge of the contact interface and outer limb edges of the armature. Significant current aggregation is also observed in the throat region of the C-shaped armature. Consequently, localized high-temperature zones develop at both the trailing contact edge and leading edge of the armature's outer limb. As shown in Figure 11, the hotspot region has covered the entire outer limb edge, and a melting zone appears at the trailing part. The propagation of this melting and ablation wave is consistent with the phenomena reported in [27] and [28].

It is observed that the temperature in these localized hotspots approaches or reaches the melting point of the armature material. To physically represent the thermal buffering effect of melting, the thermal model incorporates an isothermal phase-change approximation. In this approach, the temperature is held at the melting point once reached, while the latent heat of fusion is absorbed. This allows the simulation to identify regions undergoing phase change and quantify the energy sink effect, providing a more realistic prediction than a single-phase model. It is important to note that while this method predicts the initiation and thermal impact of melting, it does not model the subsequent fluid dynamics of the molten material, such as its flow or ejection from the contact interface, which represents a scope for future model enhancement.

7. CONCLUSION

This study establishes a finite element model for electro-magneto-thermal multiphysics coupling in pulsed high-current linear drive systems, employing localized modeling and rail reverse motion techniques. The model performs coupled calculations across physical fields on a unified mesh grid, resolving field distributions under interactions while quantifying dynamic contact resistance and heat partition mechanisms. Key conclusions from numerical simulations are: 1) The localized modeling scheme achieves efficient simulation of sliding electrical contact with reduced mesh density while satisfying current continuity constraints; 2) Contact resistance evolution is co-regulated by normal pressure, tangential friction and temperature rise, reaching its minimum during peak current periods and exhibiting significant negative correlation with electromagnetic thrust; 3) The separated interfacial heat source loading mechanism reveals strong coupling between current skin-effect zones and localized hotspots, providing theoretical foundations for thermal management. The numerical computation results demonstrate the validity of the proposed modeling approach, providing theoretical guidance for structural design optimization in high-current linear drive systems. It is important to note that the present study is primarily focused on the development and numerical validation of a multi-physics modeling framework. Direct experimental validation of the dynamic contact resistance under such extreme conditions poses significant challenges and is identified as a critical objective for future work.

REFERENCES

[1] Ma, W. and J. Lu, "Research progress and challenges of electromagnetic launch technology," *Transactions of China Electrotechnical Society*, Vol. 38, No. 15, 3943–3959, 2023.

[2] Ruan, J., L. Chen, S. Xia, Z. Wang, and L. Li, "A review of current distribution in electromagnetic railguns," *Transactions of China Electrotechnical Society*, Vol. 35, No. 21, 4423–4431, 2020.

[3] Zhang, J., J. Lu, S. Tan, Y. Zhang, and B. Li, "A magnetic diffusion model of electromagnetic launcher considering initial contact pressure," *Transactions of China Electrotechnical Society*, Vol. 37, No. 2, 488–495, 2022.

[4] James, T. E. and D. C. James, "Contact pressure distribution and transition in solid armatures [EM launchers]," *IEEE Transactions on Magnetics*, Vol. 37, No. 1, 81–85, 2001.

[5] Schneider, M., M. Woetzel, W. Wenning, and D. Walch, "The ISL rapid fire railgun project RAFIRA. Part I: Technical aspects and design considerations," *IEEE Transactions on Magnetics*, Vol. 45, No. 1, 442–447, 2009.

[6] Barber, J. P. and Y. A. Dreizin, "Model of contact transitioning with "realistic" armature-rail interface," *IEEE Transactions on Magnetics*, Vol. 31, No. 1, 96–100, 1995.

[7] Barber, J. P., A. Challita, B. Maas, and L. Thurmond, "Contact transition in metal armatures (railguns)," *IEEE Transactions on Magnetics*, Vol. 27, No. 1, 228–232, 1991.

[8] Feng, D., S. Xia, L. Chen, *et al.*, "Non-uniformity of contact pressure distribution in armature assembly for railguns," *High Voltage Engineering*, Vol. 41, No. 6, 1873–1878, 2015.

[9] Rip, L., S. Satapathy, and K.-T. Hsieh, "Effect of geometry change on the current density distribution in C-shaped arma-

tures," *IEEE Transactions on Magnetics*, Vol. 39, No. 1, 72–75, 2003.

[10] Li, C., S. Xia, L. Chen, J. He, Y. Xiong, C. Zhang, and J. Yao, "Simulations on current distribution in railgun under imperfect contact conditions," *IEEE Transactions on Plasma Science*, Vol. 47, No. 5, 2264–2268, 2019.

[11] Yang, Y., C. Fu, W. Xue, and H. Zhao, "Numerical calculation of movement electromagnetic field distribution between rail and armature," *Journal of Gun Launch & Control*, Vol. 35, No. 3, 1–5, 2014.

[12] Lin, Q. and B. Li, "Modeling and simulation of electromagnetic railgun launching process based on a transient multi-physical field solver," *Acta Armamentarii*, Vol. 41, No. 9, 1697–1707, 2020.

[13] Wu, X., X. Yang, J. Ye, and G. Liu, "Novel prognostics for IGBTs using wire-bond contact degradation model considering on-chip temperature distribution," *IEEE Transactions on Power Electronics*, Vol. 40, No. 3, 4411–4424, 2025.

[14] Coffo, M. and J. Gallant, "Simulation of the current distribution and the heat load of a brush projectile in a railgun with the finite element code ANSYS," *Acta Physica Polonica A*, Vol. 115, No. 6, 1112–1114, 2009.

[15] Li, B., J. Lu, S. Tan, Y. Zhang, and X. Cai, "Research on dynamic wear process of armature surface in high-speed sliding electric contact," *Transactions of China Electrotechnical Society*, Vol. 38, No. 1, 131–139, 2023.

[16] Hsieh, K.-T., S. Satapathy, and M.-T. Hsieh, "Effects of pressure-dependent contact resistivity on contact interfacial conditions," *IEEE Transactions on Magnetics*, Vol. 45, No. 1, 313–318, 2009.

[17] Zhu, C. and B. Li, "Analysis of sliding electric contact characteristics in augmented railgun based on the combination of contact resistance and sliding friction coefficient," *Defence Technology*, Vol. 16, No. 4, 747–752, 2020.

[18] Chen, L., J. He, Z. Xiao, S. Xia, D. Feng, and L. Tang, "Experimental study of armature melt wear in solid armature railgun," *IEEE Transactions on Plasma Science*, Vol. 43, No. 5, 1142–1146, 2015.

[19] Jaeger, J. C., "Moving sources of heat and the temperature at sliding contacts," *Journal and proceedings of the Royal Society of New South Wales*, Vol. 76, No. 3, 203–224, 1942.

[20] Siopis, M. J. and R. W. Neu, "Wear at high sliding speeds and high contact pressures," *Wear*, Vol. 342, 356–363, 2015.

[21] Yao, J. and Q. Fu, "Heat partition process at sliding electrical contact interfaces with high-speed and large current," *Transactions of China Electrotechnical Society*, Vol. 39, No. 17, 5497–5507, 2024.

[22] Chen, Y., W. Xu, W. Yuan, Y. Zhao, P. Yan, and G. Lan, "Sliding electrical contacts between aluminum armature and different material rails in railgun," *High Voltage Engineering*, Vol. 39, No. 4, 937–942, 2013.

[23] Bayati, M. S., A. Keshtkar, and A. Keshtkar, "Thermal computation in railgun by hybrid time domain technique 3-D-FEM-IEM," *IEEE Transactions on Plasma Science*, Vol. 39, No. 1, 18–21, 2011.

[24] Hsieh, K., "A Lagrangian formulation for mechanically, thermally coupled electromagnetic diffusive processes with moving conductors," *IEEE Transactions on Magnetics*, Vol. 31, No. 1, 604–609, 1995.

[25] Bayati, M. S. and K. Amiri, "Study of various C-shaped armatures in electromagnetic launcher," *Applied Computational Electromagnetics Society Journal (ACES)*, Vol. 30, No. 9, 1029–1034, 2021.

[26] Bayati, M. S. and A. Keshtkar, "Study of the current distribution, magnetic field, and inductance gradient of rectangular and circular railguns," *IEEE Transactions on Plasma Science*, Vol. 41, No. 5, 1376–1381, 2013.

[27] Sun, J., J. Cheng, Q. Wang, L. Xiong, Y. Cong, and Y. Wang, "Numerical simulation of melt-wave erosion in 2-D solid armature," *IEEE Transactions on Plasma Science*, Vol. 50, No. 4, 1032–1039, 2022.

[28] Tang, B., Y. Xu, Q. Lin, and B. Li, "Synergy of melt-wave and electromagnetic force on the transition mechanism in electromagnetic launch," *IEEE Transactions on Plasma Science*, Vol. 45, No. 7, 1361–1367, 2017.